Supplementary Information

Symmetry-Broken Kondo Screening and Zero-Energy Mode in the Kagome Superconductor CsV_3Sb_5

Yubing Tu[1,2,8], Zongyuan Zhang[1,2,3,8], Wenjian Lu[4,8], Tao Han[1,2], Run Lv[4], Zhuying Wang[5], Zekun Zhou[1], Xinyuan Hou[1,2,3], Ning Hao[6✉], Zhenyu Wang[5,7✉], Xianhui Chen[5,7], Lei Shan[1,2,3,7✉]

[1]Information Materials and Intelligent Sensing Laboratory of Anhui Province, Institutes of Physical Science and Information Technology, Anhui University, Hefei, 230601, China.

[2]Leibniz International Joint Research Center of Materials Sciences of Anhui Province, Anhui University, Hefei, 230601, China.

[3]Center of High Magnetic Fields and Free Electron Lasers, Anhui University, Hefei, 230601, China.

[4]Key Laboratory of Materials Physics, Institute of Solid State Physics, HFIPS, Chinese Academy of Sciences, Hefei, 230031, China.

[5]Department of Physics, CAS Key Laboratory of Strongly-coupled Quantum Matter Physics, University of Science and Technology of China, Hefei, Anhui 230026, China

[6]Anhui Provincial Key Laboratory of Low-Energy Quantum Materials and Devices, High Magnetic Field Laboratory, HFIPS, Chinese Academy of Sciences, Hefei, 230031, China.

[7]Hefei National Laboratory, University of Science and Technology of China, Hefei 230088, China

[8]These authors contributed equally: Yubing Tu, Zongyuan Zhang, Wenjian Lu.

✉Email: haon@hmfl.ac.cn; zywang2@ustc.edu.cn; lshan@ahu.edu.cn

Section 1. Identification of Ta and Cr dopants

To identify the artificial dopants, STM images were collected at different bias voltages. At a setting bias of +1.5 V, Ta and Cr dopants appear as bright protrusions on the exposed Sb1 surface, centered around the V site beneath the Sb1 layer (Fig. S1a, b), similar to the case of Ti dopants [1]. Other types of defects could be distinguished from Ta or Cr dopants in the low-bias topographies shown in Fig. S1e-i. The concentration of Ta or Cr dopants could be determined by counting the number of dopants in a given area. The actual doping concentration of the Ta-doped samples was characterized using an energy-dispersive spectrometer (EDS), while the concentration of the Cr-doped samples was obtained through inductively coupled plasma atomic emission spectroscopy (ICP-AES), which is more accurate for determining the much lower concentration of Cr. The results obtained from EDS and ICP-AES are summarized in Table S1.

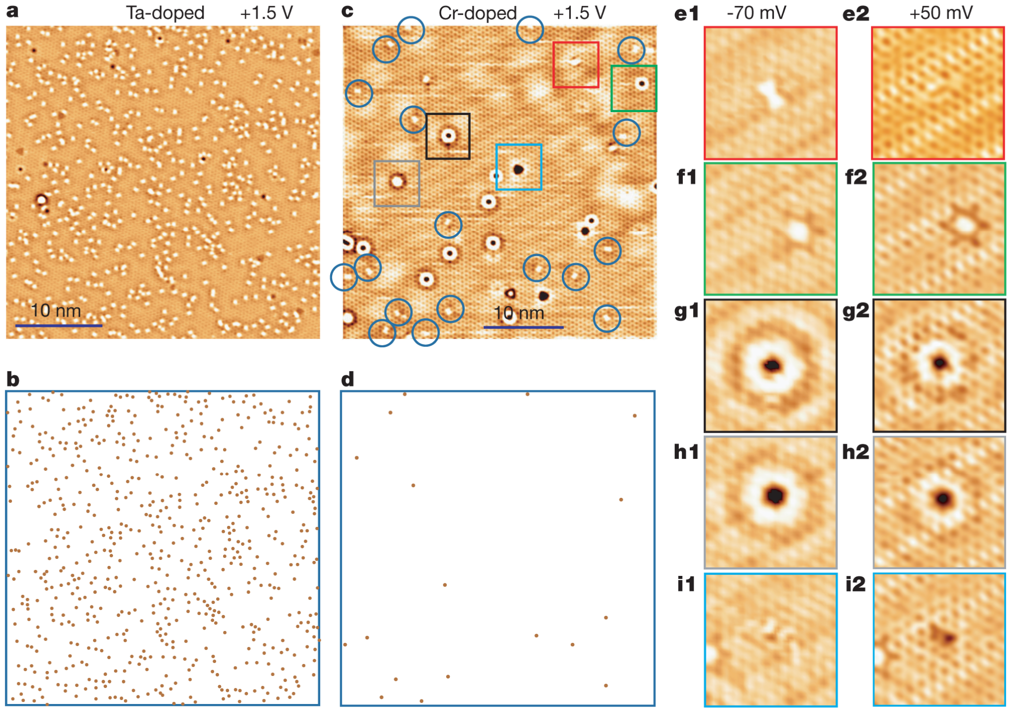

Fig. S1 Determination of the concentrations of Ta and Cr dopants. a, c, Typical STM topographies of CsV$_{2.925}$Ta$_{0.075}$Sb$_5$ and CsV$_{2.997}$Cr$_{0.003}$Sb$_5$. The bright protrusions represent Ta or Cr atoms that substitute for V atoms in the underlying kagome layer. **b, d,** Distributions of dopant atoms in the field of view shown in (**a**) and (**c**). The numbers of Ta and Cr atoms, determined by counting are 646 and 18, respectively. **e-i**, Five types of defects other than Cr, framed in the colored boxes in (**c**). The STM setup conditions: V_s = +1.5 V, I_t = 300 pA (**a**); V_s = +1.5 V, I_t = 100 pA (**c**); V_s = -70 mV, I_t = 200 pA(**e1**); V_s = +50 mV, I_t = 200 pA (**e2**); V_s = -70 mV, I_t = 200 pA (**f1**); V_s = +50 mV, I_t = 200 pA (**f2**); V_s = -70 mV, I_t = 200 pA (**g1**); V_s = +50 mV, I_t = 200 pA (**g2**); V_s = -70 mV, I_t = 200 pA (**h1**); V_s = +50 mV, I_t = 200 pA (**h2**); V_s = -70 mV, I_t = 200 pA (**i1**); V_s = +50 mV, I_t = 200 pA (**i2**).

$CsV_{3-x}Ta_xSb_5$ (EDS)	**Sb(%)**	**V(%)**	**Cs(%)**	**Ta(%)**	**x**
Sample1	56	32.4	10.8	0.8	0.082
Sample2	56.1	31.8	11.3	0.8	0.074
Sample3	59.5	30.2	9.6	0.8	0.077

$CsV_{3-x}Cr_xSb_5$ (ICP-AES)	**V(μg/ml)**	**Cr(μg/ml)**	**x**
sample1	0.9515434133	0.000942623387	0.0029
sample2	7.13418753	0.009454423	0.0038
sample3	3.683985708	0.003141433	0.0025

Table S1 Concentrations of Ta and Cr dopants. The Ta concentration was characterized using EDS, while the Cr concentration was determined by ICP-AES for trace amounts.

Section 2. Resistance measurements

The samples were characterized though electrical resistivity measurements, as shown in Fig. S2. The superconducting transition temperature T_c (where resistance drops to zero) was determined to be 3.0 K for both pristine CsV_3Sb_5 and $CsV_{2.925}Ta_{0.075}Sb_5$, and 2.6 K for $CsV_{2.997}Cr_{0.003}Sb_5$. The CDW transition temperature (T_{CDW}), indicated by the arrows, was found to be 93 K for pristine CsV_3Sb_5, while 81 K and 91 K for the Ta-doped and Cr-doped samples respectively, consistent with previous studies [2, 3].

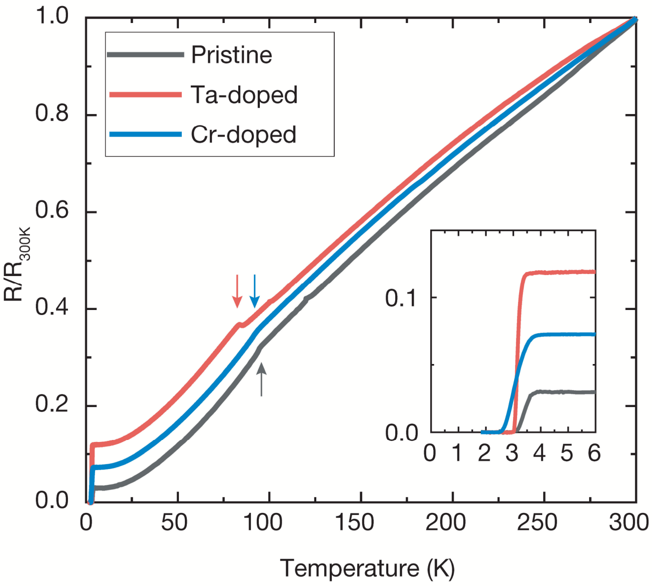

Fig.S2 Transport properties of the pristine and Ta-, Cr-doped CsV_3Sb_5 samples. Temperature-dependent in-plane resistance of the pristine and Ta, Cr-doped CsV_3Sb_5 crystals, normalized to the data at 300 K. Inset: A zoomed-in view of the low-temperature part, highlighting the superconducting transition.

Section 3. Native non-magnetic Sb-site defects

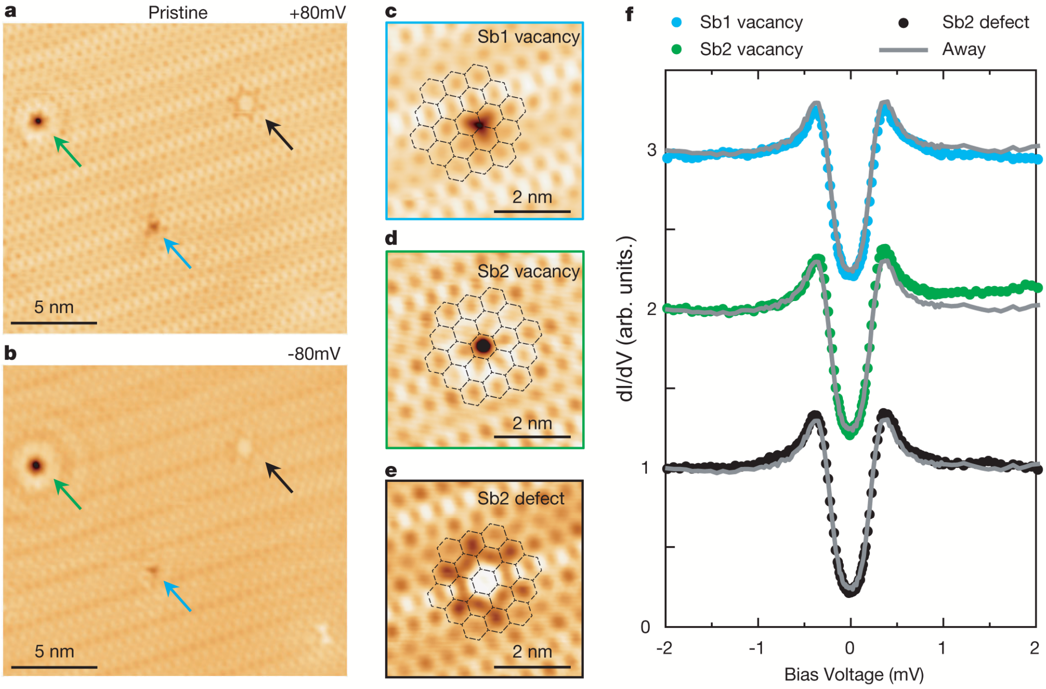

Fig.S3 Identification of Sb defects. a, b, STM topographies accquired in the same area of pristine CsV_3Sb_5 at different bias voltages. **c-e,** Atomically resolved STM topographies of the Sb1 vacancy (**c**), Sb2 vacancy (**d**) and Sb2 defect (**e**), as indicated by arrows in (a) and (b). **f**, Spectra taken on top of and away from the Sb1 vacancy, Sb2 vacancy and Sb2 defect. The STM setup conditions: V_s = +80 mV I_t = 500 pA (**a**); V_s= -80 mV I_t = 500 pA (**b**); V_s = +80 mV I_t = 300 pA (**c**); V_s = +80 mV I_t = 200 pA (**d**); V_s = +80 mV I_t = 200 pA (**e**); V_s = -5 mV, I_t = 300 pA, V_m = 0.05 mV, T = 0.4 K (**f**).

Section 4. Kondo effect of various Cr dopants

To reveal the commonality of Kondo effect in the Cr-doped CsV_3Sb_5, dI/dV spectra measurements were performed around various Cr sites, yielding a similar symmetry-broken pattern at the Kondo resonance energies as shown in Fig. S4. It was noted that the resonance energies are distributed between -2.5 meV and +5.5 meV. We also compared the pairing potential (superconducting gap) and Kondo energy, as described in the text. By fitting the spectra taken away from impurities to the Dynes model [4] with different gap functions, the paring potential was determined to be $\Delta \sim 0.29$ meV (for an isotropic gap), $\Delta_{max} \sim 0.38$ meV (for an anisotropic gap) and $\Delta_1 \sim 0.25$ meV, $\Delta_2 \sim 0.35$ meV (for multiple gaps), as shown in Fig. S5a. The Kondo temperature, proportional to the Kondo energy, can be determined to be $T_K = 18$ K by fitting the spectra to a single Fano function [5], as presented in Fig. S5b. In addition, the orientation of the Kondo patterns was compared with that of the coexistent $4a_0$ modulations as shown in Fig. S6. The lack of correlation between them indicates that the symmetry breaking of the Kondo pattern is not due to the uniaxial charge order. Moreover, a strain analysis as shown in Fig. S7 excludes the strain effect as the origin of such unique Kondo pattern.

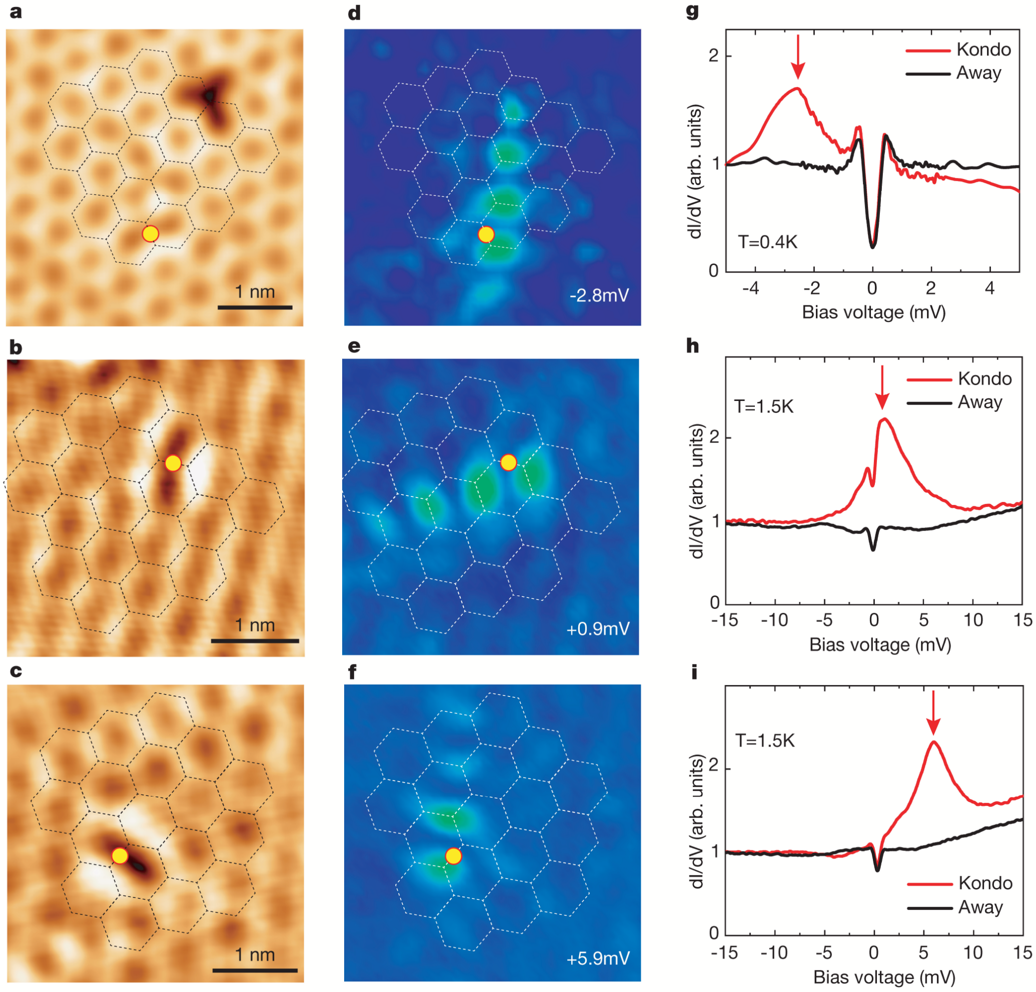

Fig.S4 Kondo states around three individual Cr dopants. a-c, STM topographies of three Cr dopants. **d-f**, dI/dV map for the Cr dopants shown in (**a-c**). The yellow dots indicate the exact locations of the Cr dopants. **g-i**, dI/dV spectra taken at the positions with maximum intensity of Kondo resonance, and away from the Cr dopants. STM setup conditions: V_s = -500 mV, I_t = 100 pA (**a**); V_s = -80 mV, I_t = 40 pA (**b**); V_s = +80 mV, I_t = 20 pA (**c**); V_s = -5 mV, I_t = 300 pA, V_m = 0.05 mV, T = 0.4 K (**g**); V_s = -20 mV, I_t = 300 pA, V_m = 0.2 mV, T = 1.5 K (**h**); V_s = -20 mV, I_t = 300 pA, V_m = 0.2 mV, T = 1.5 K (**i**).

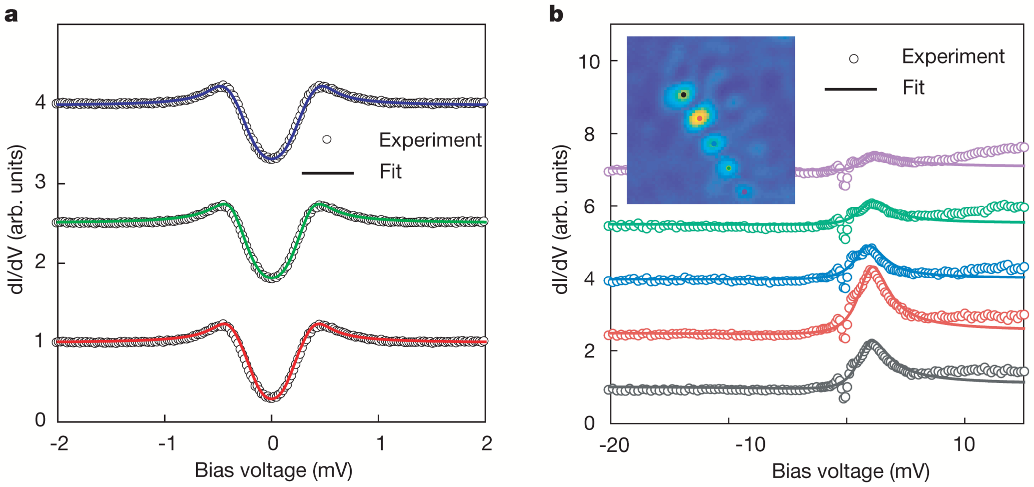

Fig. S5 Evaluations of pairing potential and Kondo energy. a, Tunneling spectra obtained far from the impurities (circles), and the fitting results with different superconducting gap functions (isotropic s-wave: blue, anisotropic s-wave: green, two-gap isotropic s-wave: red). **b,** The main panel shows the tunneling spectra (circles) measured at different locations indicated by the dots with the same colors as that of corresponding spectra (inset). Solid lines are the fitting results according to a Fano lineshape. The spectra are vertically offset for clarity.

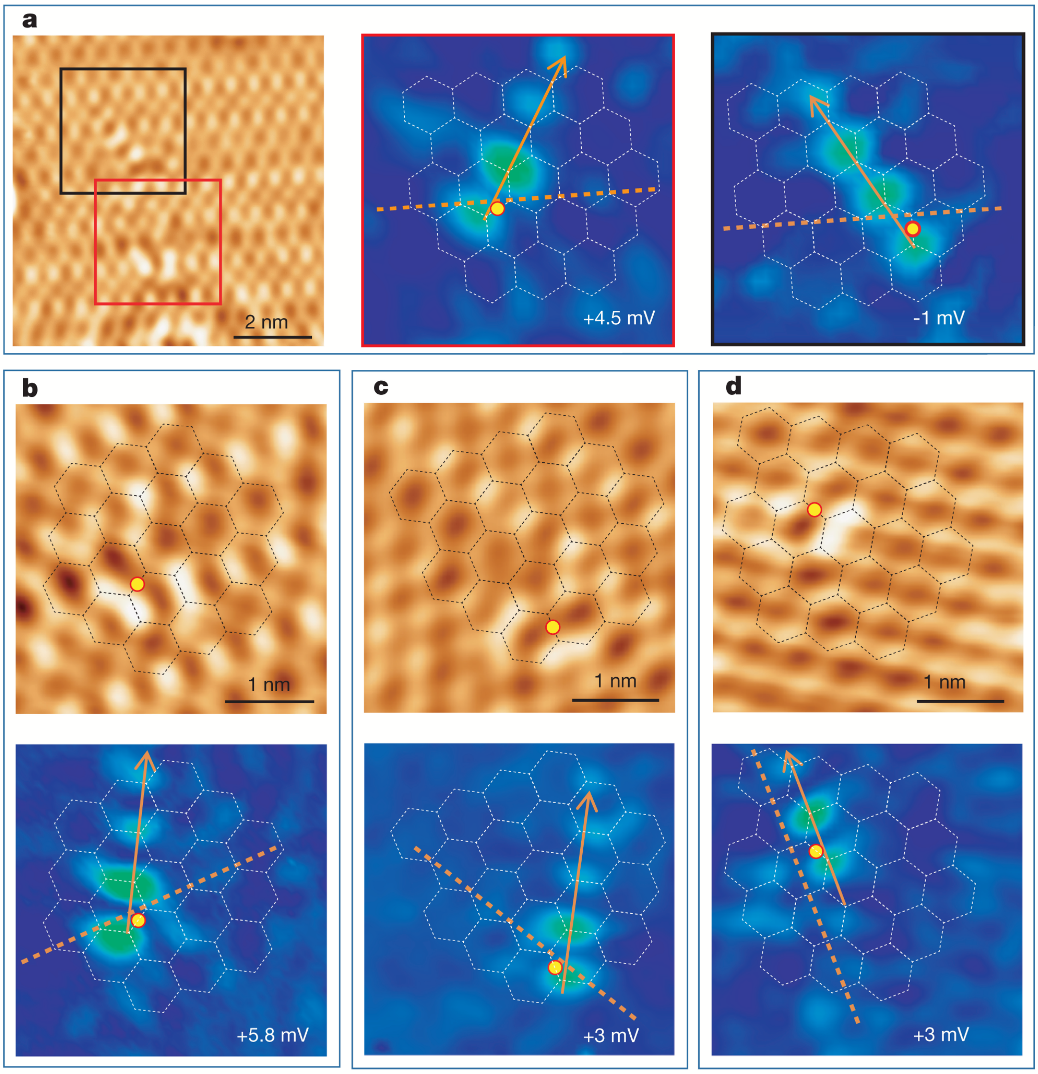

Fig.S6 Symmetry-broken patterns along different directions relative to that of the 4a$_0$ modulations. **a**, STM topography and dI/dV mappings of two nearby Cr dopants. **b-d**, STM topographies and dI/dV maps of three individual Cr dopants on the same surface. Orange dotted lines indicate the direction of 4a$_0$, and orange arrows indicate the spatial patterns of Kondo screening. STM setup conditions: V_s = -80 mV, I_t = 50 pA (**a**); V_s = -80 mV, I_t = 1 nA (**b**); V_s = -85 mV, I_t = 1 nA (**c**); V_s = -80 mV, I_t = 50 pA (**d**).

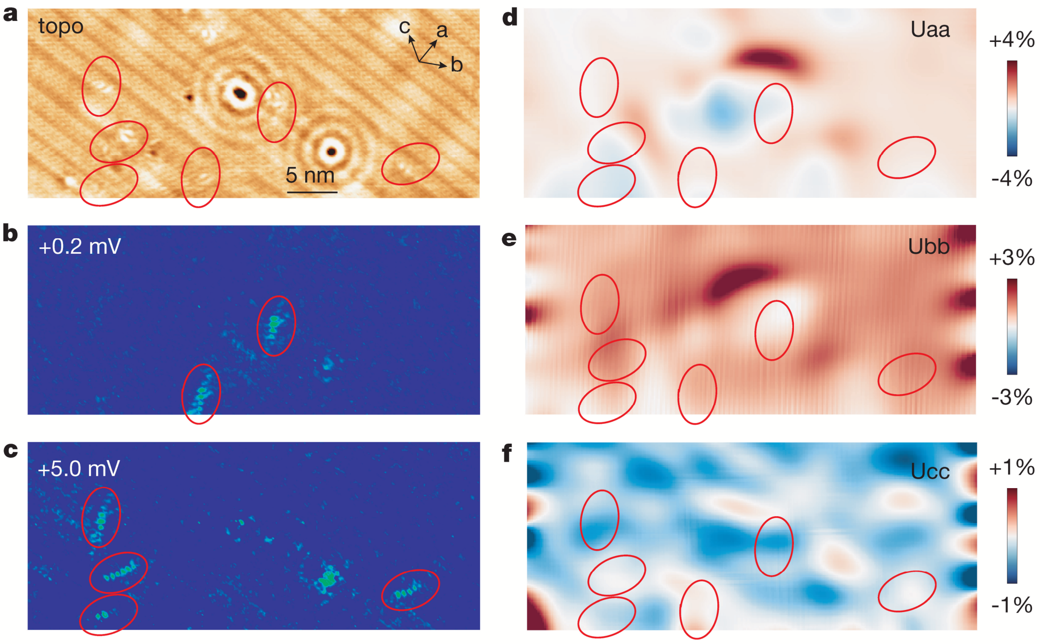

Fig. S7. Strain analysis. a, STM topography containing several Cr dopants. **b, c**. dI/dV maps for the Cr dopants in (**a**) at +0.2 mV and +5.0 mV, respectively. **d-f**, Uaa, Ubb, Ucc maps obtained from the topography in (**a**), indicating the strain field along the axes of a, b, and c, respectively.

Section 5. Identification of the V vacancies in both pristine and doped samples

By considering the small displacements of the two Sb1 atoms adjacent to a V vacancy (Fig. S8a), the dumbbell-shaped defect observed in our STM images (Fig. 3a,b) can be well reproduced by DFT simulations for different biases as shown in Fig. S8b,c. Such V vacancies exist in both pristine and doped samples with extremely low concentrations, most likely produced during crystal synthesis. Spectrally, they can be characterized by a hump at a negative energy of approximately -100 meV in the local density of states (LDOS) as illustrated in Fig. S8g-l. This is in contrast to Ta dopants, which show almost unchanged LDOS in the same energy range, and is also different from the case of Cr dopants showing a Kondo peak around zero energy.

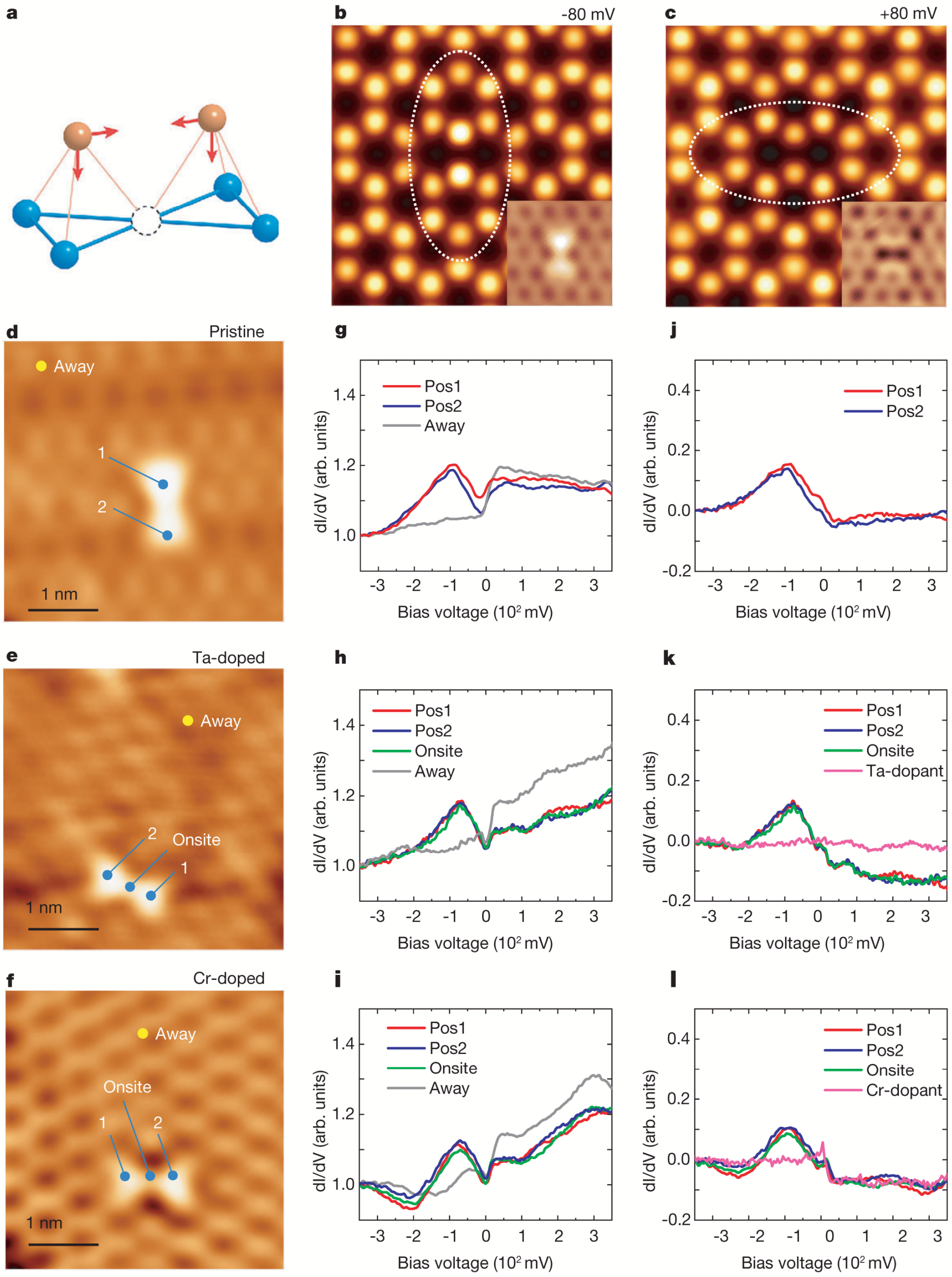

Fig. S8 STM Topographies and dI/dV spectra of V vacancies in pristine and doped samples. a, Schematic of a V vacancy. The red arrows indicate the displacements of nearby Sb1 atoms. **b**, **c**, Comparison of theoretical simulations with STM topographies (insets) obtained at a negative bias (**b**) and a positive bias (**c**). **d-f,** STM topographies acquired in pristine (**d**), Ta-doped (**e**) and Cr-doped (**f**) CsV_3Sb_5. **g-i**, dI/dV spectra taken on top of and away from the dumbbell-shaped V vacancies in pristine (**d**), Ta-doped (**e**) and Cr-doped (**f**) CsV_3Sb_5. **j-l,** The same spectra of V vacancies as that in (g)-(i), by subtracting the backgrounds marked as "Away" for comparison, the spectra (with the background subtracted) of a Ta dopant and a Cr dopant are also shown in (**k**) and (**l**), respectively. The STM setup conditions: V_s = -80 mV, I_t = 50 pA (**b** inset); V_s = +80 mV, I_t = 50 pA (**c** inset); V_s = -100 mV, I_t = 20 pA (**d**); V_s = -100 mV, I_t = 20 pA (**e**); V_s = -100 mV, I_t = 30 pA (**f**); V_s = -1 V, I_t = 300 pA, V_m=10 mV, T=0.4 K (**g**); V_s = -500 mV, I_t = 300 pA, V_m=5 mV, T=0.4 K (**h**); V_s = -500 mV, I_t = 300 pA, V_m=5 mV, T=4.2 K (**i**).

Section 6. Temperature and magnetic field dependence of the dI/dV spectra of V vacancies

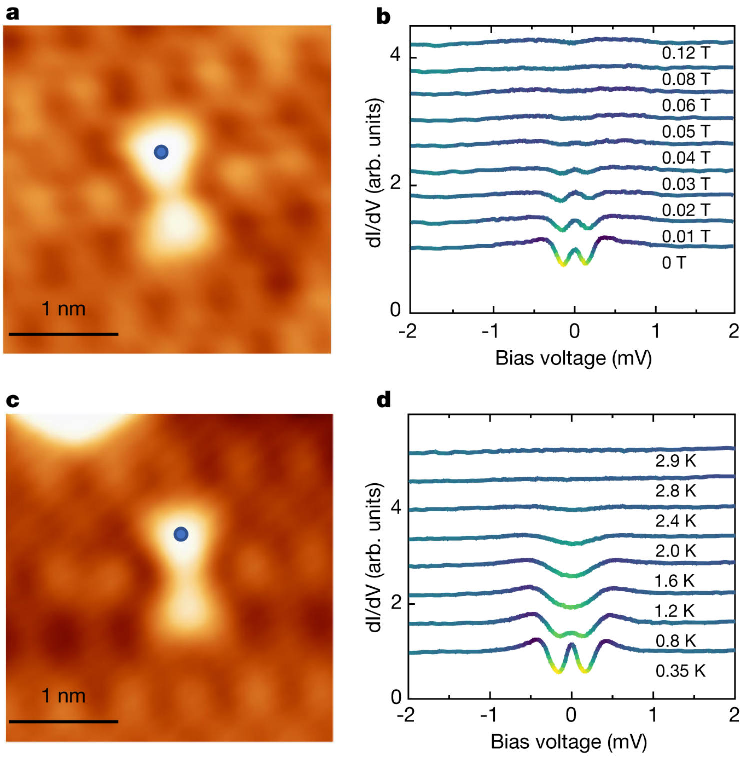

Fig. S9 Perturbation of the ZBS by temperature and magnetic field. a, b, Spectra taken at a V vacancy in pristine material at different vertical magnetic fields. **c, d**, Spectra taken at another V vacancy in pristine material at different temperatures. STM setup conditions: V_s = -80 mV, I_t = 20 pA (**a**); V_s = -5 mV, I_t = 300 pA, V_m= 0.05 mV, T = 0.4 K (**b**); V_s = -80 mV, I_t = 20 pA (**c**); V_s = -5 mV, I_t = 300 pA, V_m = 0.05 mV, B = 0 T, (**d**).

Section 7. Influence of impurities on magnetic properties

To investigate the influence of the V vacancies on magnetic properties, we first evaluated it from an energetic perspective. The total energy of the spin-polarized state is approximately 22 meV lower than that of the non-spin-polarized state. In the spin-polarized state, the vacancy-nearest neighbor V atoms show a magnetic moment of 0.14 μ_B, while the next-nearest neighbor V atoms display an antiparallel magnetic moment of -0.1 μ_B. The magnetic moments of the farther V atoms progressively weaken, with alternating spin orientations. This behavior is consistent with expectations for Ruderman-Kittel-Kasuya-Yosida exchange interactions. We also calculated the magnetic properties of Ti-, Cr- and Ta-doped CsV_3Sb_5. For the Ti- and Ta-doped cases, DFT self-consistent calculations converge to the non-magnetic state. For the Cr-doped case, the total energy of the spin-polarized state is lower than that of the non-spin-polarized state by approximately 106 meV, indicating a stable magnetic configuration. The Cr atom exhibits a magnetic moment of 1.62 μ_B. The Cr-nearest and next-nearest neighbor V atoms show magnetic moments of -0.13 μ_B and +0.01 μ_B, with alternating spin orientation, similar to the V- vacancy case.

Section 8. Coexistence of zero-energy bound states (ZBSs) and YSR states

In order to investigate the detailed changes in the LDOS induced by a V vacancy, we plotted the difference between the dI/dV spectra taken along the lines crossing a V vacancy (from Fig. 3e,f) and that measured far away from the vacancy, as shown in Fig. S10a,b. This method has often been adopted to identify magnetic impurity induced YSR states both in conventional superconductors and iron-based superconductors [6-8]. These difference spectra reveal a pair of humps with symmetric energies relative to the Fermi level, characteristic of the YSR resonance, coexisting with the ZBCP. Similar coexistence was observed in both Ta- and Cr-doped samples, as shown in Fig. S10c,d, although the YSR peaks may be less pronounced in some instances due to their small spectral weight.

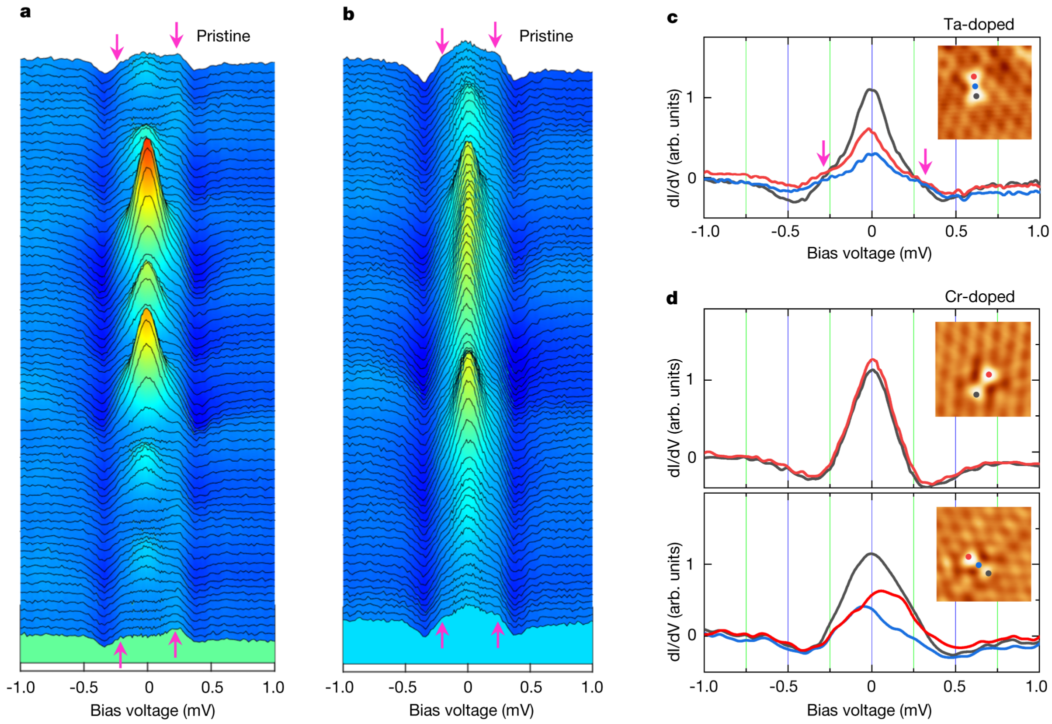

Fig. S10 Difference spectra obtained around V vacancies of pristine and doped CsV$_3$Sb$_5$. a, **b**, Spectra presented in Fig. **3e,f** of the main text after background subtraction. **c**, Difference spectra of a V vacancy in Ta-doped CsV$_3$Sb$_5$. **d**, Difference spectra of two V vacancies in Cr-doped CsV$_3$Sb$_5$. magenta arrows indicate the features of YSR states. The background used to obtain the difference spectra in each case was measured on the clean Sb surface about 30 Å away from the vacancies. The STM setup conditions: V_s = -80 mV, I_t = 20 pA (**c** insert); V_s = -40 mV, I_t = 20 pA (**d** upper insert); V_s = -100 mV, I_t = 100 pA (**d** lower insert).

Supplementary References

[1] Wu, P., Tu, Y., Wang, Z. et al. Unidirectional electron–phonon coupling in the nematic state of a kagome superconductor. *Nat. Phys.* **19**, 1143–1149 (2023).

[2] Zhong, Y., Liu, J., Wu, X. et al. Nodeless electron pairing in CsV_3Sb_5-derived kagome superconductors. *Nature* **617**, 488–492 (2023).

[3] Ding, G., Wo, H. L., Gu, Y. Q. et al. Effect of chromium doping on superconductivity and charge density wave order in the kagome metal $Cs(V_{1-x}Cr_x)_3Sb_5$. *Phys. Rev. B* **106**, 235151 (2022).

[4] R. C. Dynes, V. Narayanamurti, & J. P. Garno, Direct Measurement of Quasiparticle-Lifetime Broadening in a Strong-Coupled Superconductor, *Phys. Rev. Lett.* **41**, 1509 (1978).

[5] Madhavan, V., Chen, W., Crommie M. F. & Wingreen N. S. Tunneling into a Single Magnetic Atom: Spectroscopic Evidence of the Kondo Resonance. *Science* **280**, 567-569 (1998).

[6] Yazdani, A., Lutz, C. P. & Eigler D. M. Probing the local effects of magnetic impurities on superconductivity. *Science* **275**,1767-1770 (1997).

[7] Yang, H., Wang, Z., Fang, D. et al. In-gap quasiparticle excitations induced by non-magnetic Cu impurities in $Na(Fe_{0.96}Co_{0.03}Cu_{0.01})As$ revealed by scanning tunnelling spectroscopy. *Nat. Commun.* **4**, 2749 (2013).

[8] Liu, X., Tao, R., Ren, M. et al. Evidence of nematic order and nodal superconducting gap along [110] direction in $RbFe_2As_2$. *Nat. Commun.* **10**, 1039 (2019).